




Functional specificity of liquid-liquid phase separation at the synapse

Received: 12 March 2024

Accepted: 8 November 2024

Published online: 21 November 2024

 Check for updatesNatalie J. Guzikowski^{1,2} & Ege T. Kavalali^{1,2}  

The mechanisms that enable synapses to achieve temporally and spatially precise signaling at nano-scale while being fluid with the cytosol are poorly understood. Liquid-liquid phase separation (LLPS) is emerging as a key principle governing subcellular organization; however, the impact of synaptic LLPS on neurotransmission is unclear. Here, using rat primary hippocampal cultures, we show that robust disruption of neuronal LLPS with aliphatic alcohols severely dysregulates action potential-dependent neurotransmission, while spontaneous neurotransmission persists. Synaptic LLPS maintains synaptic vesicle pool clustering and recycling as well as the precise organization of active zone RIM1/2 and Munc13 nanoclusters, thus supporting fast evoked Ca^{2+} -dependent release. These results indicate although LLPS is necessary within the nanodomain of the synapse, the disruption of this nano-organization largely spares spontaneous neurotransmission. Therefore, properties of in vitro micron sized liquid condensates translate to the nano-structure of the synapse in a functionally specific manner regulating action potential-evoked release.

The synapse, a highly ordered and dynamic subcellular system, maintains autonomy, organization, and high-fidelity neurotransmission without a bounding membrane. Unlike other cellular substructures (i.e., the nucleus, mitochondria, endoplasmic reticulum), the synapse does not possess an enclosing membrane to aid in compartmentalization. Despite this, the synapse is still able to orchestrate numerous, distinct functional pathways fundamental in larger-scale brain circuits and higher order processing. Over the past decade, a growing amount of research has revealed how liquid-liquid phase separation (LLPS) mediates protein interactions throughout the cell and furthermore, at the synapse^{1–5}. However, whether the phase separation properties of synaptic proteins maintain or even contribute to the temporal and spatial specificity of neurotransmission remains to be elucidated.

LLPS is a process by which liquid condensates enriched in specific protein-protein or protein-nucleic acid complexes separate from a de-enriched dilute phase, creating distinct phases within the cytosol⁶. Intrinsically disordered regions (IDRs) of proteins lack a stably folded secondary and tertiary structure and therefore do not

from site specific stoichiometric interactions, however, specific physicochemical principles mediate their multivalent interactions, including but not limited to hydrophobic, electrostatic, cation- π , π - π , and weakly polar interactions, to create enriched pockets of proteins that are spatially distinct from the cytosol^{6–11}. Multi-component complexes formed by macromolecules with both folded domains and IDRs results in the coupling of transition properties with associative site specific interactions (percolation) and segregative transitions (phase separation)^{6,11,12}. Since one third of the eukaryotic genome contains proteins with IDRs, it follows that numerous synaptic proteins have liquid-like properties and phase separate in vitro⁸. However, how the abundance of in vitro micron-sized synaptic condensate evidence reconciles with the nanometer level organization of the synapse is unclear.

The benchmarks for establishing protein phase separation include analyzing droplet properties, assessing fluorescence recovery after photobleaching, and the application of the aliphatic alcohol, 1,6-hexanediol (1,6-HD) to dissolve liquid condensates^{13,14}. To translate the abundance of in vitro data demonstrating the phase separation

¹Department of Pharmacology, Vanderbilt University, Nashville, TN, USA. ²Vanderbilt Brain Institute, Vanderbilt University, Nashville, TN, USA.

✉ e-mail: ege.kavalali@vanderbilt.edu

capabilities of numerous synaptic proteins to a functional role of LLPS in synaptic signaling, we utilized aliphatic alcohols in a neuronal culture system to determine the relationship between liquid condensates and the nanoscale organization of the synapse.

Initially we took an unbiased approach utilizing aliphatic alcohols to target hydrophobic LLPS interactions at the synapse; revealing phase separation mediated functional specificity is vital in regulating different modes of neurotransmission. Subsequently we delineated pre-synaptic structural deficits mediating evoked release susceptibility and spontaneous neurotransmission resilience to LLPS perturbation in synaptic vesicle pool clustering/recycling and active zone organization. Here, we show RIM1 LLPS is vital in regulating the efficacy and integrity of fast evoked calcium dependent release whereby active zone nano-cluster liquid condensates facilitate evoked release independent of spontaneous release. Ultimately revealing how the dynamic equilibrium of proteins in the liquid state is fundamental in mediating phase separation's utility within the nanoscale micro-environment of the synapse.

Results

Sub-nuclear membrane-less condensates mediated by hydrophobic interactions are well reported to phase separate^{14–17}. Therefore, to establish our ability to disrupt phase separation in hippocampal neurons with 3% 1,6-HD we examined a well-defined nuclear structure that phase separates, nuclear speckles. Consistent with the literature, upon 1,6-HD treatment, the number of nuclear speckles present within the nucleus were reduced (Fig. 1a–d)¹⁵. Throughout this study, we take advantage of 1,6-HD and other aliphatic alcohols to differentiate between liquid condensates and solid-like complexes to specifically manipulate LLPS assemblies independent of structured domain interactions¹⁴.

LLPS is necessary for action potential-dependent neurotransmission

The synapse is a directional network vital for information flow, where LLPS is involved in protein organization at every level of neurotransmission: synaptic vesicle pool clustering^{3,18–21}, active zone scaffolding^{22,23}, active zone assembly²⁴, synaptic vesicle endocytosis^{25,26}, and inhibitory and excitatory post-synaptic density scaffolding^{27–29}. Despite compelling evidence that synaptic proteins phase separate, it has been challenging to determine if the liquid condensate properties of these proteins are necessary, and ultimately essential to the function of the synapse.

To address this, action potential-dependent (evoked) neurotransmission was monitored during 3% 1,6-HD wash-on to quantify the evoked response over time by regular stimulation at 0.1 Hz (Fig. 1e). Strikingly, excitatory and inhibitory evoked neurotransmission rapidly diminished within one minute of 1,6-HD application (to 10% for evoked inhibitory postsynaptic currents (eIPSCs) and 15% for evoked excitatory postsynaptic currents (eEPSCs) of their initial amplitude). Upon 1,6-HD washout, the evoked signal quickly recovered to the strength of the initial response (Fig. 1e–h). To validate these results with 1,6-HD, we also employed 1,5-pentanediol (1,5-PD) and 2,5-hexanediol (2,5-HD) due to the rank order of their liquid condensate melting activity; 1, 6-HD > 1,5-PD > 2,5-HD¹⁵. Treatment with 1,5-PD similarly resulted in the robust dysregulation of evoked neurotransmission as eEPSCs diminish to less than 50% and eIPSCs to ~30%, albeit at a longer time course (Fig. 1i–l). This loss of evoked current is specific to identified *in vitro* modulators of LLPS, i.e., linear carbon chains with terminal groups, as it is mimicked by 3% 1,6-hexanedithiol (1, 6-HDT) and 3% 1,7-HD, as well as 4, 4'-dianilino-1, 1'-binaphthyl-5, 5'-disulfonic acid (bis-ANS), a chemically unique modulator of LLPS but not 2,5-hexanediol (2,5-HD) (Fig. 1m–p, Supplementary Fig. 1a–h)^{15,19,30}. In addition to the reduced evoked amplitude, 1,6-HD and 1,5-PD treatment slowed the rise time of eIPSCs relative to 2,5-HD treatment (Fig. 1q–s, Supplementary Fig. 1i–l),

suggesting a sub-synaptic structural property might be disrupted upon melting of liquid condensates. With application of aliphatic alcohols, 1,6-HD, 1,5-PD, and 2,5-HD, there is a moderate decline in membrane resistance; however, this effect appears independent of the documented neurotransmission deficits (Supplementary Fig. 2a–d)¹⁴.

While the segregation of evoked and spontaneous neurotransmission has been repeatedly demonstrated, the majority of proteins necessary for release and post-synaptic signaling overlap^{31–38}. To ascertain whether disruption of LLPS has a universal effect on all modes of neurotransmission, we quantified spontaneous neurotransmission following acute 3% 1,6-HD or 3% 1,5-PD wash-on and subsequent wash-off. Surprisingly, spontaneous neurotransmission was generally resistant to 1,6-HD application, as mEPSC frequency was maintained, while amplitudes were decreased; mIPSC frequency was reduced by ~50%, while amplitudes were unchanged (Fig. 2a–c, f–h, Supplementary Fig. 3f, g). Similarly, application of 1,5-PD and 1,7-HD resulted in an augmentation of mEPSC frequency and decrease in mEPSC amplitude (Fig. 2k–m, Supplementary Fig. 3a–e). Unlike evoked neurotransmission, spontaneous neurotransmission showed no change in kinetics reflected in rise and decay times of individual events (Fig. 2d, e, i, j, n, o), illustrating the preservation of spontaneous release events and kinetics despite disruption of phase separation.

Notably, recently identified *in vitro* liquid like properties of synapsin are consistent with the observed inhibitory and excitatory spontaneous neurotransmission phenotype. For instance, the divergent effect of aliphatic alcohols on inhibitory vs. excitatory spontaneous release resembles the synapsin triple knockout synaptic phenotype³⁹, where liquid-like properties are suggested to mediate synaptic vesicle pool clustering^{18–21}. In sum, following global LLPS disruption spontaneous neurotransmission is reasonably maintained compared to the near negligible amount of remaining evoked current with altered kinetics.

Spontaneous neurotransmission persists despite melting of synaptic condensates

Until this point 1,6-HD was applied only acutely due to its rapid effect on evoked fusion properties and the potential deleterious effects of prolonged 1,6-HD treatment in an *in vivo* system¹⁴. However, to ascertain if spontaneous neurotransmission is truly resistant to this robust disruption of LLPS, or if a longer application of 1,6-HD would impair the structure and protein organization necessary to maintain spontaneous release, we recorded from individual cells throughout a 40-minute treatment. Consistent with the acute wash-on experiments, mEPSCs persisted throughout the duration of the recording (Fig. 3a,b, Supplementary Fig. 3h).

Due to their stochastic nature, spontaneous release events are relatively rare at individual synapses compared to stimulated evoked release³⁵. To examine if spontaneous neurotransmission is differently dependent on LLPS for synaptic organization, or if its resilience to melting is a consequence of its low frequency, we utilized different fusion machinery molecular manipulations to augment mEPSCs (Fig. 3c)⁴⁰. Relative to control (empty vector expression), Synaptotagmin 1 knockdown (Sytl KD) and expression of Synaptosomal-Associated Protein 25 kDa (SNAP25) L50S variant increased mEPSC frequency by ~4 times, moreover, SNAP25 D166Y variant increased mEPSC frequency by ~40 times, with SNAP25 D116Y baseline frequencies reaching above 50 Hz (Fig. 3d–e, Supplementary Fig. 3i)⁴⁰.

Regardless of baseline mEPSC frequency, in the presence of 3% 1,6-HD, mEPSCs were maintained with a slightly augmented frequency and decreased amplitude (Fig. 3f–n). Interestingly, mEPSC frequency reached the highest average release rate under 1,6-HD conditions, with a mean of 62.67 Hz for SNAP25 D166Y, potentially nearing a threshold for the rate of spontaneous release (Fig. 3m). Despite global disruption to LLPS with 1,6-HD, an extremely high degree of spontaneous exocytosis and subsequent vesicle recycling is maintained, suggesting that

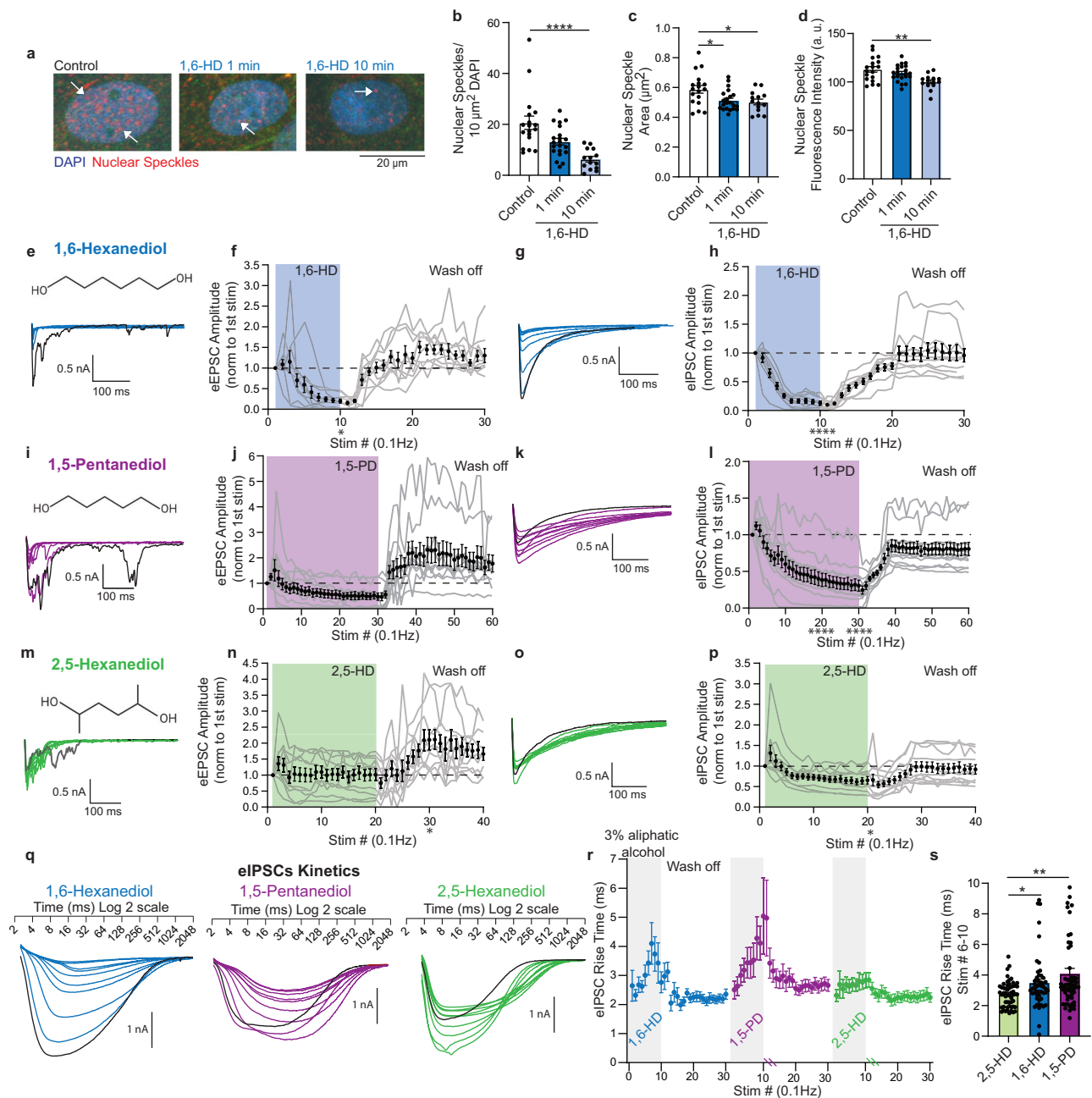


Fig. 1 | Action potential-dependent neurotransmission is disrupted following LLPS manipulation. **a** Nuclear speckle staining (images are maximum intensity projections from z-stacks). **b**, Number of nuclear speckles per 10 μ m² of DAPI, **c** nuclear speckle area and **d** nuclear speckle fluorescence intensity (control $n = 15$, 1 min $n = 21$, 10 min $n = 14$ ROIs). **e** Representative traces of eEPSCs during 3% 1,6-HD wash on, first trace in black. **f** eEPSC amplitude during treatment ($n = 10$ cells). **g** Representative traces of eEPSCs during 3% 1,6-HD wash on, first trace in black. **h** eEPSC amplitude during treatment ($n = 10$ cells). **i** Representative traces of eEPSCs during 3% 1,5-PD wash on, first trace in black. **j** eEPSC amplitude during treatment ($n = 10$ cells). **k** Representative traces of eEPSCs during 3% 1,5-PD wash on, first trace in black. **l** eEPSC amplitude during treatment ($n = 12$ cells). **m** Representative traces of eEPSCs during 3% 2,5-HD wash on, first trace in black. **n** eEPSC amplitude during treatment ($n = 10$ cells). **o** Example traces of eEPSCs during 3% 2,5-HD wash on, first trace in black. **p** eEPSC amplitude during treatment ($n = 11$ cells). **q** Sample traces of

eEPSC kinetics following 3% aliphatic alcohol treatment, first stimulation in black. **r** Analysis of eEPSC rise times (20–80%) with 3% aliphatic alcohol treatment during wash-on for ten stimulations, followed by a 20 stimulation wash-off period (stimulation events not included are in Supplementary Fig. 1j–l, to compare same treatment length) (1,6-HD $n = 10$, 1,5-PD $n = 12$, 2,5-HD $n = 11$ cells). **s** Comparison of eEPSC rise times for stimulation #6–10 (period when see robust amplitude effect) during 3% aliphatic alcohol treatment (1,6-HD $n = 50$, 1,5-PD $n = 60$, 2,5-HD $n = 55$ stimulation events). Values are mean \pm SEM. Significance reported as: * $p < 0.05$, ** $p < 0.01$, *** $p < 0.001$, and **** $p < 0.0001$. Statistical analyses conducted were one-way Kruskal-Wallis test with Dunn's multiple comparisons test (**b**, **s**), one-way ANOVA with Dunnett's multiple comparison test (**c**, **d**), one-way Friedman test with Dunn's multiple comparisons test comparing amplitude to the 1st stimulation every ten stimulations (**f**, **h**, **j**, **l**, **n**, **p**). Source data are provided as a source data file. Exact p -values reported in Supplementary Data 1.

the SNARE machinery is intact to support augmented spontaneous neurotransmission. To further probe vesicle recycling dynamics, we inhibited the vacuolar-ATPase with folimycin and prevented vesicle refilling (Fig. 3c); resulting in a significant decrease in mEPSC

frequency and amplitude that is not recapitulated by comparable 1,6-HD treatment (Fig. 3o–q). Ultimately demonstrating that vesicle recycling is necessary to maintain high frequency spontaneous release^{41,42} but liquid condensates are not. These results suggest that a

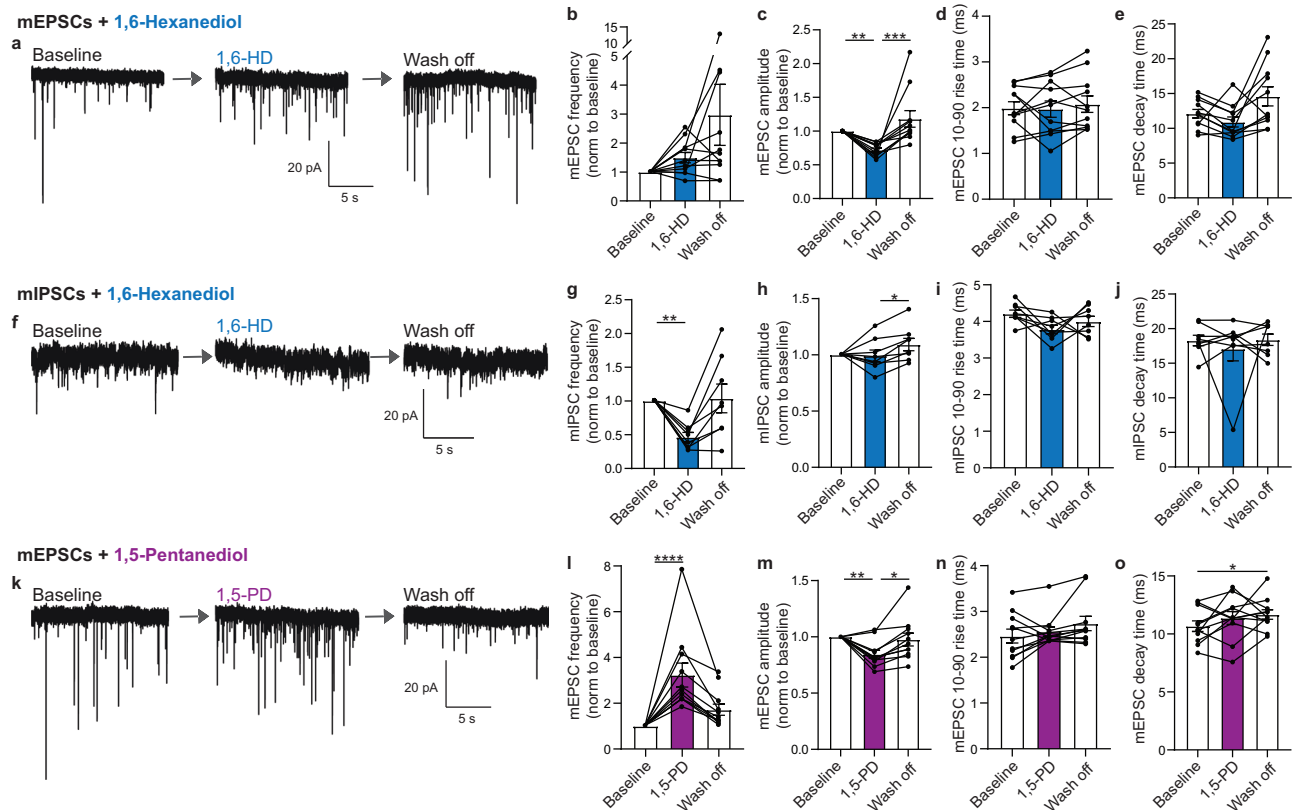


Fig. 2 | Spontaneous neurotransmission persists despite LLPS disruption.

a Example traces of mEPSCs at baseline, 2 min 3% 1,6-HD treatment, and during wash off. **b** Analysis of mEPSC frequency normalized to baseline, **c** mEPSC amplitude normalized to baseline, **d** mEPSC event rise times (10–90), and **e** mEPSC event decay times ($n = 11$ cells). **f** Example traces of mIPSCs at baseline, 2 min 3% 1,6-HD treatment, and during wash off. **g** Analysis of mIPSC frequency normalized to baseline, **h** mIPSC amplitude normalized to baseline, **i** mIPSC event rise times (10–90), and **j** mIPSC event decay times ($n = 8$ cells). **k** Example traces of mEPSCs at

baseline, 2 min 3% 1,5-PD treatment, and during wash off. **l** Analysis of mEPSC frequency normalized to baseline, **m** mEPSC amplitude normalized to baseline, **n** mEPSC event rise times (10–90), and **o** mEPSC event decay times ($n = 11$ cells). Values are mean \pm SEM. Significance reported as: * $p < 0.05$, ** $p < 0.01$, *** $p < 0.001$, and **** $p < 0.0001$. Statistical analyses conducted were one-way Friedman test with Dunn's multiple comparisons test (**b**, **c**, **g**, **h**, **j**, **l**–**n**) and one-way ANOVA with Tukey's multiple comparison test (**d**, **e**, **i**, **o**). Source data are provided as a source data file. Exact p -values reported in Supplementary Data 1.

fundamental mechanism driving evoked neurotransmission is supported via phase separation, but it is not necessary for spontaneous quantal release.

Disrupting LLPS disorders synaptic vesicle pool clustering and dynamics

Phase separation complexes are implicated throughout the synaptic vesicle cycling pathway, providing an explanation to the seemingly contradictory phenotype of tightly clustered synaptic vesicle (SV) pools that are also highly dynamic^{3,43}. To examine the readily releasable pool (RRP), hypertonic sucrose was perfused and both the excitatory and inhibitory RRP response were recorded (Fig. 4a, b). Upon LLPS disruption, there was a reduction in the amplitude of the excitatory but not the inhibitory RRP (Fig. 4b–e). Despite having no physical boundaries to define synaptic vesicle pool organization, primary central synapses have an almost stereotyped SV pool cluster shape, a spherical cluster near the active zone (Fig. 4a). With high resolution dSTORM imaging, we observed an effect on both the glutamate and GABA containing synaptic vesicle pools, marked by their respective vesicular transporters, with a reduction in volume and a loss of spherical shape following one minute 3% 1,6-HD treatment, with a more robust effect on the GABA synaptic vesicle pool (Fig. 4f–i, l–n, raw example images Supplementary Fig. 4a, b). This data is consistent with previously reported LLPS mediated interactions between synapsin and synaptophysin in SV pool clustering^{18–20}. To examine if these changes in vesicle pool organization have a functional effect on SV

pool replenishment and recycling, neurons were stimulated at 10 Hz for 250 stimulations following one minute 1,6-HD perfusion. Excitatory evoked responses exhibited an increase in release probability and faster rate of depression upon repetitive prolonged stimulation (Fig. 4j, k), whereas inhibitory evoked responses displayed a decreased release probability with a slower rate of depression relative to control (Fig. 4o, p).

Surprisingly, the *in vitro* identification of proteins that phase separate, including synapsin, synaptophysin, piccolo, dynamin splice isoform dyn1xA, Eps15 and fcho1/2, corresponds with the deficits in vesicle pool organization, recycling, and endocytosis observed here, providing compelling evidence for the functional relevance of LLPS^{18–20,25,26,44}. This synaptic vesicle pool phenotype implicates synapsin phase separation as the main driver of the marginal changes in mPSC frequency and amplitude upon disruption to LLPS³⁹. However, the described alterations in SV pool dynamics do not sufficiently resolve the difference in fusion competence between evoked and spontaneous release reflected in changes in both the RRP size and ePSC kinetics.

Calcium-dependent release relies on nanoscale active zone LLPS complexes

To elucidate the structural correlate to this functional deficit, we dissected putative pre- and post-synaptic components of our electrophysiological observations. First, we demonstrated that the 1,6-HD treatment effect is not use-dependent, as evoked response amplitudes

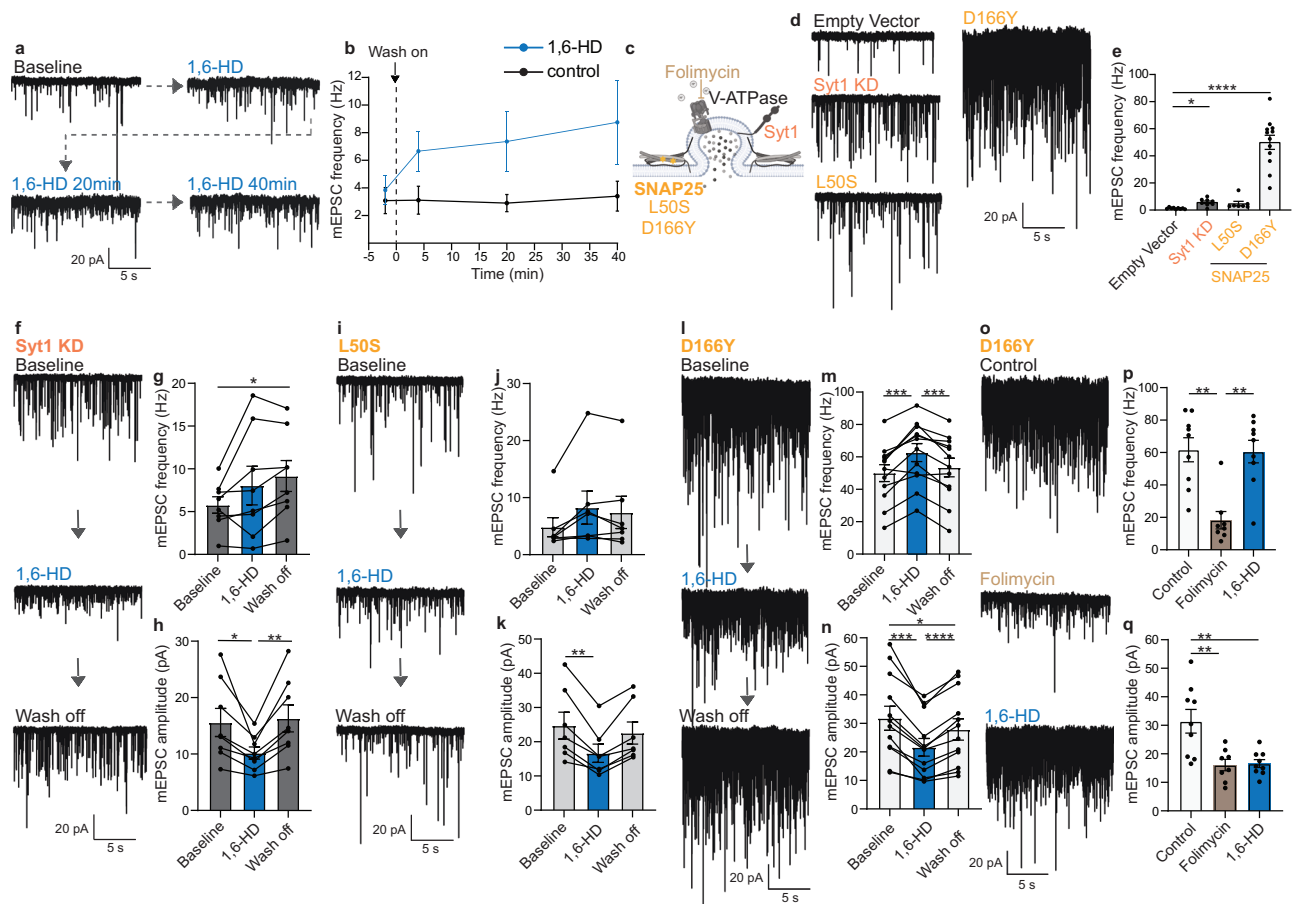


Fig. 3 | Genetic augmentation of spontaneous neurotransmission during LLPS disruption. **a** Example mEPSC traces at baseline, immediately following 3% 1,6-HD application, after 20 minutes, and 40 minutes of 3% 1,6-HD exposure to the same cell. **b** Analysis of mEPSC frequency over time with continued exposure to 3% 1,6-HD (1,6-HD $n = 5$, control $n = 5$ cells). **c** Schematic of fusing synaptic vesicle with V-ATPase, Synaptotagmin 1 (Syt1), and Synaptosomal-Associated Protein 25 kDa (SNAP25) variants L50S and D166Y (Created in BioRender. Guzikowski, N. (2024)). **d** Example mEPSC traces of four groups including empty vector (control), Synaptotagmin 1 knockdown (Syt1 KD), SNAP25 L50S variant, and SNAP25 D166Y variant. **e** Analysis of baseline mEPSC frequency of Syt1 KD and two SNAP25 genetic variants (Empty Vector $n = 9$, Syt1 KD $n = 8$, L50S $n = 7$, D166Y $n = 12$ cells, same data used for baseline in 1,6-HD treatment experiments). **f–n** Across the three different genetic backgrounds representative traces and quantification of 2 min 3% 1,6-HD treatment

on mEPSC frequency and amplitude (Syt1 KD $n = 8$, L50S $n = 7$, D166Y $n = 12$ cells). **o** Example mEPSC traces of control (DMSO), 10 minute folimycin pre-treatment (also included in the bath), and 10 minute 1,6-HD treatment in the D166Y SNAP25 genetic background. **p** Analysis of mEPSC frequency and **q** mEPSC amplitude (control $n = 9$, folimycin $n = 8$, 1,6-HD $n = 9$ cells). Values are mean \pm SEM. Significance reported as: * $p < 0.05$, ** $p < 0.01$, *** $p < 0.001$, and **** $p < 0.0001$. Statistical analyses conducted were unpaired two tailed t-test or two tailed t-test Mann-Whitney test performed between groups at baseline, 4 min, 20 min, and 40 min intervals (**b**), one-way Kruskal-Wallis test with Dunn's multiple comparisons test (**e**, **p**), one-way ANOVA with Dunnett's/Tukey's multiple comparison test (**g**, **h**, **m**, **n**, **q**), one-way Friedman test with Dunn's multiple comparisons test (**j**, **k**). Source data are provided as a source data file. Exact p -values reported in Supplementary Data 1.

diminish independent of stimulation during 3% 1,6-HD application (Supplementary Fig. 5a). To delineate a post-synaptic mechanism 3% 1,6-HD was included in the patch pipette internal solution. Under this condition eIPSC amplitudes and rise time kinetics were unchanged relative to control (Fig. 5a–c, Supplementary Fig. 5b). Furthermore, when the 1,6-HD concentration was increased to 10%, or neurons were dialyzed for up to 45 minutes, there was no difference between 1,6-HD and controls (Fig. 5c, Supplementary Fig. 5b, c). These results suggest a primarily pre-synaptic mechanism is driving the alternations in evoked release kinetics, vesicle recycling, and RRP size.

Evoked and spontaneous neurotransmission have differential Ca^{2+} dependencies, with the nanoscale coupling of clustered voltage gated Ca^{2+} channels (VGCCs) at synaptic vesicle release sites fundamental in the ultra-fast nature of action potential-dependent release⁴⁵. Upon perfusion of a high concentration potassium external solution, 3% 1,6-HD drastically reduced the amount of Ca^{2+} -dependent release (Fig. 5d, e). Likewise, when a Ca^{2+} indicator tagged to synaptic vesicles, Syb2-GCaMP8s, was used to detect Ca^{2+} currents, the peak Ca^{2+}

response to high potassium perfusion at individual boutons was also reduced (Fig. 5f–h, Supplementary Fig. 6a, b). This seems to be a direct effect of LLPS disruption on Ca^{2+} channel organization, and not proximity of the vesicle to VGCCs, as the results are nearly identical when using soluble GCaMP8f (Supplementary Fig. 6c–f). When action potential dynamics are quantified during 1,6-HD treatment, action potentials cannot be evoked, despite large current injections (Supplementary Fig. 7a–c). The inability to generate action potentials is most likely due to the inhibition of sodium conductance through voltage gated sodium channels by 1,6-HD^{46,47}. Independent of action potentials, the direct synaptic measurement of the Ca^{2+} signal with GCaMP and subsequent electrophysiological measure of Ca^{2+} -dependent vesicle fusion upon high concentration potassium perfusion establishes that the strength of the pre-synaptic Ca^{2+} signal at the active zone relies on a LLPS mediated mechanism.

To further investigate whether the loss of evoked release integrity is due to the structural organization of Ca^{2+} signals within the pre-synapse we conducted eIPSCs recordings in an elevated Ca^{2+} bath

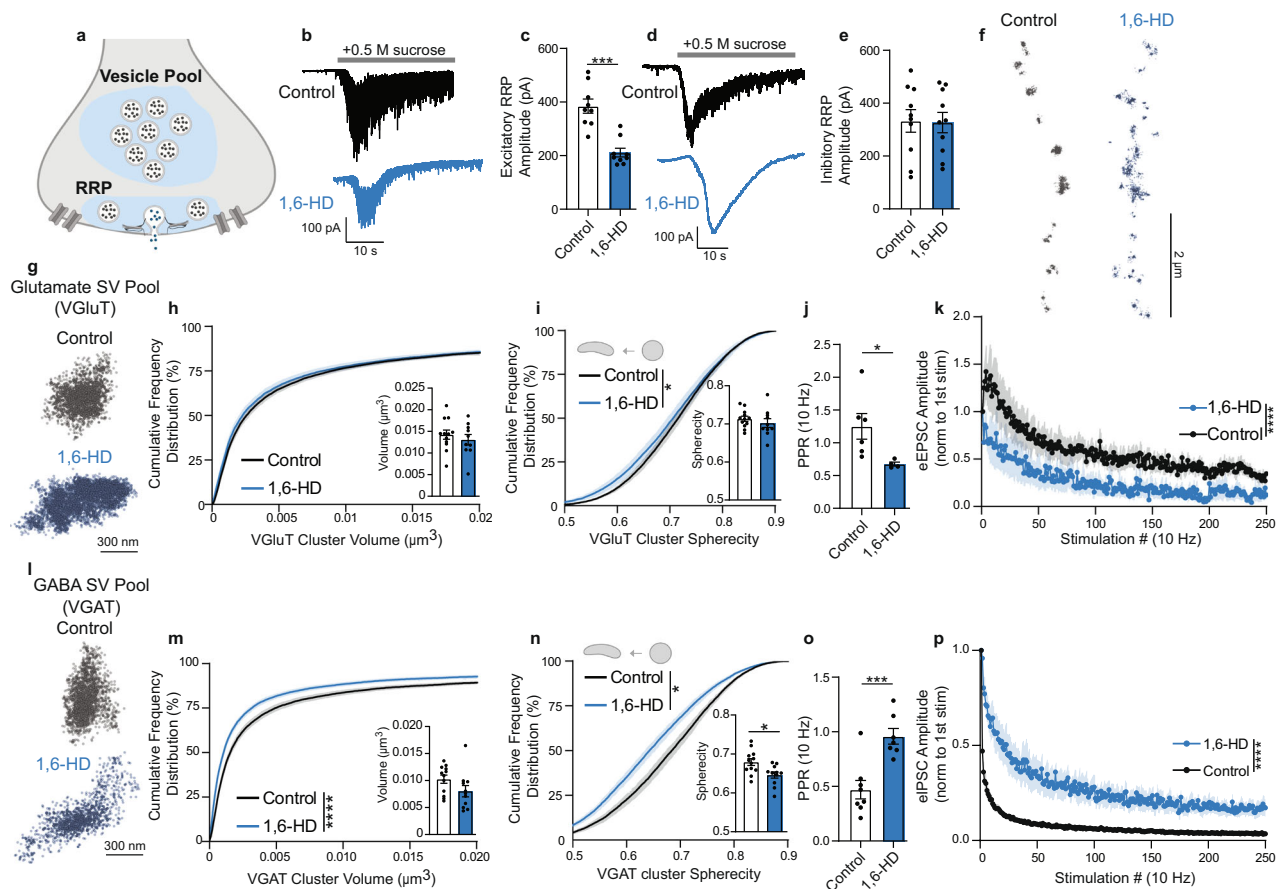


Fig. 4 | Synaptic vesicle pool clustering dynamics altered with liquid condensate melting. **a** Diagram of vesicle pools within the pre-synapse (Created in BioRender. Guzikowski, N. (2023)). **b** Representative traces of excitatory RRP upon 0.5 M sucrose perfusion. **c** Peak amplitude of 0.5 M sucrose response ($n = 9$ cells). **d** Representative traces of inhibitory RRP upon 0.5 M sucrose perfusion. **e** Peak amplitude of 0.5 M sucrose response ($n = 10$ cells). **f** Representative image of dSTORM glutamate SV pool clusters along an axon. **g** Single cluster of dSTORM VGLuT single molecule localizations representing the glutamate containing SV pool at an individual bouton. **h** Cumulative frequency histogram of VGLuT cluster volume for all synapses with inlaid bar graph of ROI averages (control $n = 12$, 1,6-HD $n = 10$ ROIs). **i** Cumulative frequency histogram of VGLuT cluster sphericity of all synapses with inlaid bar graph of ROI averages (control $n = 12$, 1,6-HD $n = 10$ ROIs). **j** ePPSC PPR and (**k**) ePPSC amplitude during repetitive stimulation (only evoked currents large enough to differentiate from stimulation artifact and baseline activity included in analysis, 1st and 2nd stim data from Fig. 4k

used for PPR) (control $n = 6$, 1,6-HD $n = 4$ cells). **l** Single cluster of dSTORM VGAT single molecule localizations representing the GABA containing SV pool at an individual bouton. **m** Cumulative frequency histogram of VGAT cluster volume of all synapses with an inlaid bar graph of ROI averages (control $n = 12$, 1,6-HD $n = 11$ ROIs). **n** Cumulative frequency histogram of VGAT cluster sphericity of all synapses with an inlaid bar graph of ROI averages (control $n = 12$, 1,6-HD $n = 11$ ROIs). **o** ePPSC PPR and (**p**) ePPSC amplitude during repetitive stimulation (only evoked currents large enough to differentiate from stimulation artifact and baseline activity included in analysis, 1st and 2nd stim data from Fig. 4p used for PPR) (control $n = 8$, 1,6-HD $n = 7$ cells). Values are mean \pm SEM. Significance reported as: * $p < 0.05$, ** $p < 0.01$, *** $p < 0.001$, and **** $p < 0.0001$. Statistical analyses conducted were two-tailed Mann-Whitney test (**c**), two-tailed unpaired t test (**e**, **h**, **i**, **j**, **m**–**o**), and Kolmogorov-Smirnov test (**h**, **i**, **k**, **m**, **n**, **p**). Source data are provided as a source data file. Exact p -values reported in Supplementary Data 1.

solution. In 8 mM Ca^{2+} the decrease in eIPSC amplitudes upon 1,6-HD treatment is not as robust or as fast compared to physiological 2 mM Ca^{2+} (Fig. 5i–j). However, in 8 mM Ca^{2+} eIPSCs still slow with 1,6-HD treatment (Fig. 5k), suggesting the tight clustering of VGCCs is disrupted as reflected in eIPSC kinetics but the greater Ca^{2+} influx partially counteracts some of the structural disorganization caused when liquid condensates are melted, as reflected in the eIPSC amplitude. While we cannot rule out a direct effect of aliphatic alcohols on VGCCs, multiple experimental results associated with evoked neurotransmitter release cannot be solely accounted for by a simple reduction in the Ca^{2+} current. For instance, the increase in the rise time of evoked events, the decrease in hypertonic sucrose evoked glutamate release and responses to 10 Hz repetitive stimulation, all indicate additional pre-synaptic targets of 1,6-HD. Furthermore, spontaneous release is partially Ca^{2+} dependent relying on a distinct population of VGCCs^{48–50}, suggesting an organizational as opposed to functional impact of 1,6-HD on VGCCs. Taken together, regardless of altered ion channel

conduction, dysregulated evoked fusion kinetics and properties suggest the molecular machinery necessary for fast release relies on LLPS.

Active zone scaffolding and organization are fundamental in action potential-dependent neurotransmission, mediating steps from synaptic vesicle priming to subsequent fusion by tightly controlling Ca^{2+} signals. VGCCs are tethered and clustered within the active zone via their direct binding to RIM (N- and P/Q-type VGCCs) and RIM-binding proteins (RIM-BPs) (L- and N-type VGCCs)^{51–53}. Consequently, the in vitro phase separation of RIM1/2 and RIM-BP on membrane bilayers induces VGCC clustering^{22,54}. Furthermore, additional active zone scaffolding proteins, Munc13 and Liprin- α 3, form liquid condensates together with RIM, suggesting that the phase separation of active zone scaffolds is potentially necessary for the clustering of VGCCs near primed vesicles to enable fast synchronous release^{23,45,55–58}.

To probe this premise, we conducted super resolution imaging of active zone scaffolds. Volume and sphericity measurements of both Munc13 and RIM1/2 synaptic clusters show modest changes in synaptic

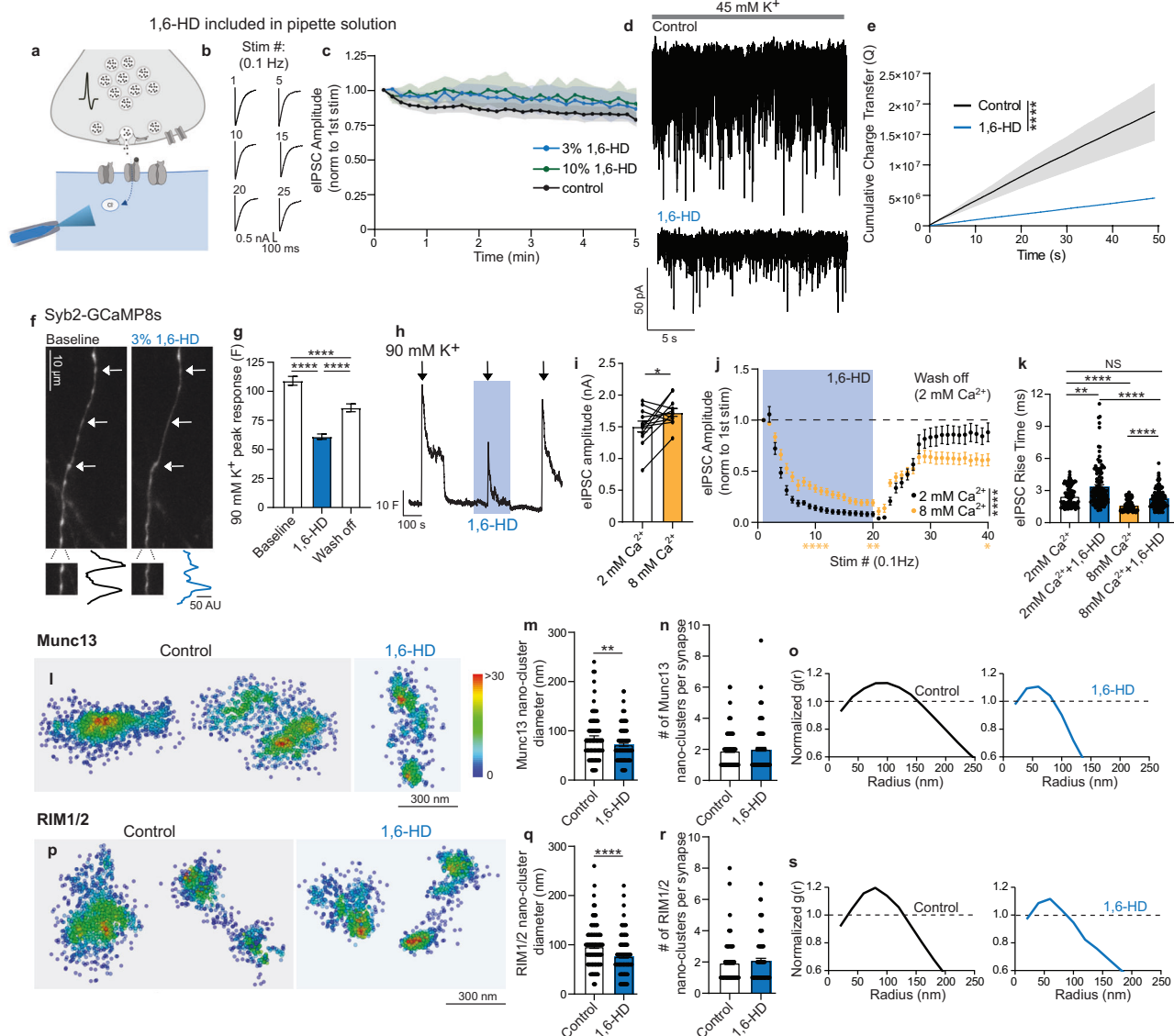


Fig. 5 | Necessity of liquid condensates in active zone nanostructure for calcium-dependent release. **a** Experimental set-up for 1,6-HD included in patch pipette internal solution (Created in BioRender. Guzikowski, N. (2023)). **b** Example traces of eIPSCs. **c** Analysis of eIPSC amplitude when aliphatic alcohols are included in the internal solution (control $n = 8$, 3% $n = 5$, 10% $n = 4$ cells, stats performed at minute interval). **d** Examples traces of whole cell voltage clamp during 45 mM K^+ perfusion. **e** Cumulative charge transfer during 45 mM K^+ perfusion following 1 min control or 3% 1,6-HD pre-treatment (with TTX, APV, Bicuculline) (control $n = 8$, 1,6-HD $n = 9$ cells). **f** Example images of axons transfected with Syb2-GCaMP8s. Arrows denote pre-synaptic boutons identified with 90 mM K^+ . Insets below represent fluorescence intensity peaks at individual boutons. **g** Peak fluorescence response ($n = 687$ boutons). **h** Example fluorescence trace (ROI average of all boutons). **i** Paired comparison of eIPSC amplitude ($n = 12$ cells, same recordings used in Fig. 5j, k). **j** eIPSC amplitude during 3% 1,6-HD wash-on and wash-off (statistical analysis comparing nonlinear fit during drug wash on and average amplitudes compared between groups at every 10th stim) (wash-off is 2 mM Ca^{2+} for both groups) (2 mM Ca^{2+} $n = 12$, 8 mM Ca^{2+} $n = 12$ cells). **k** Analysis of eIPSC rise times (20–80%) (1st 10 stim of treatment or baseline per cell included). **l** dSTORM

Munc13 single molecule localizations at an individual bouton color coded based on density heat map. **m** Munc13 nanocluster diameters (Control $n = 129$, 1,6-HD $n = 137$ synapses) and **n** number of munc13 nanoclusters per synapse (Control $n = 121$, 1,6-HD $n = 132$ synapses). **o** Normalized pair correlation function ($g(r)$) of an individual synapse. **p** dSTORM RIM1/2 single molecule localizations at an individual bouton color coded based on density heat map. **q** RIM1/2 nanocluster diameters (Control $n = 146$, 1,6-HD $n = 134$ synapses) and **r** number of RIM1/2 nanoclusters per synapse (Control $n = 132$, 1,6-HD $n = 121$ synapses). **s** Normalized pair correlation function ($g(r)$) of an individual synapse. Values are mean \pm SEM. Significance reported as: * $p < 0.05$, ** $p < 0.01$, *** $p < 0.001$, and **** $p < 0.0001$. Statistical analyses conducted were one-way ANOVA with Tukey's multiple comparison test (**c**) Simple linear regression (**e**) one-way Friedman test with Dunn's multiple comparisons test (**g**) two-tailed paired t-test (**i**) two-tailed Mann-Whitney test (**j**, **m**, **n**, **q**, **r**) two-tailed unpaired t-test (**j**), Nonlinear fit (one phase decay) comparison of fit—extra sum-of-squares F test (**j**) and one-way Kruskal-Wallis test with Dunn's multiple comparisons test (**k**). Source data are provided as a source data file. Exact p -values reported in Supplementary Data 1.

cluster organization upon one minute 3% 1,6-HD treatment (Supplementary Fig. 8a–f, raw example images in Supplementary Fig. 4c, d). However, more interestingly, within a single active zone RIM1/2 and Munc13 showed a heterogeneous molecular organization whereby an increased density of single molecules relative to overall cluster density created subsynaptic nanoclusters (Fig. 5l, p). The location of RIM1/2

nanoclusters can predict evoked fusion location and corresponds in size to post-synaptic density scaffolding and receptor clusters^{59–63}. When we disrupted LLPS complexes acutely, Munc13 and RIM1/2 nanocluster size decreased by ~20 nm, equivalent to synaptic vesicle-VGCC coupling distance^{64–68}; altering the alignment and positioning of active zone machinery necessary for synaptic vesicle priming and

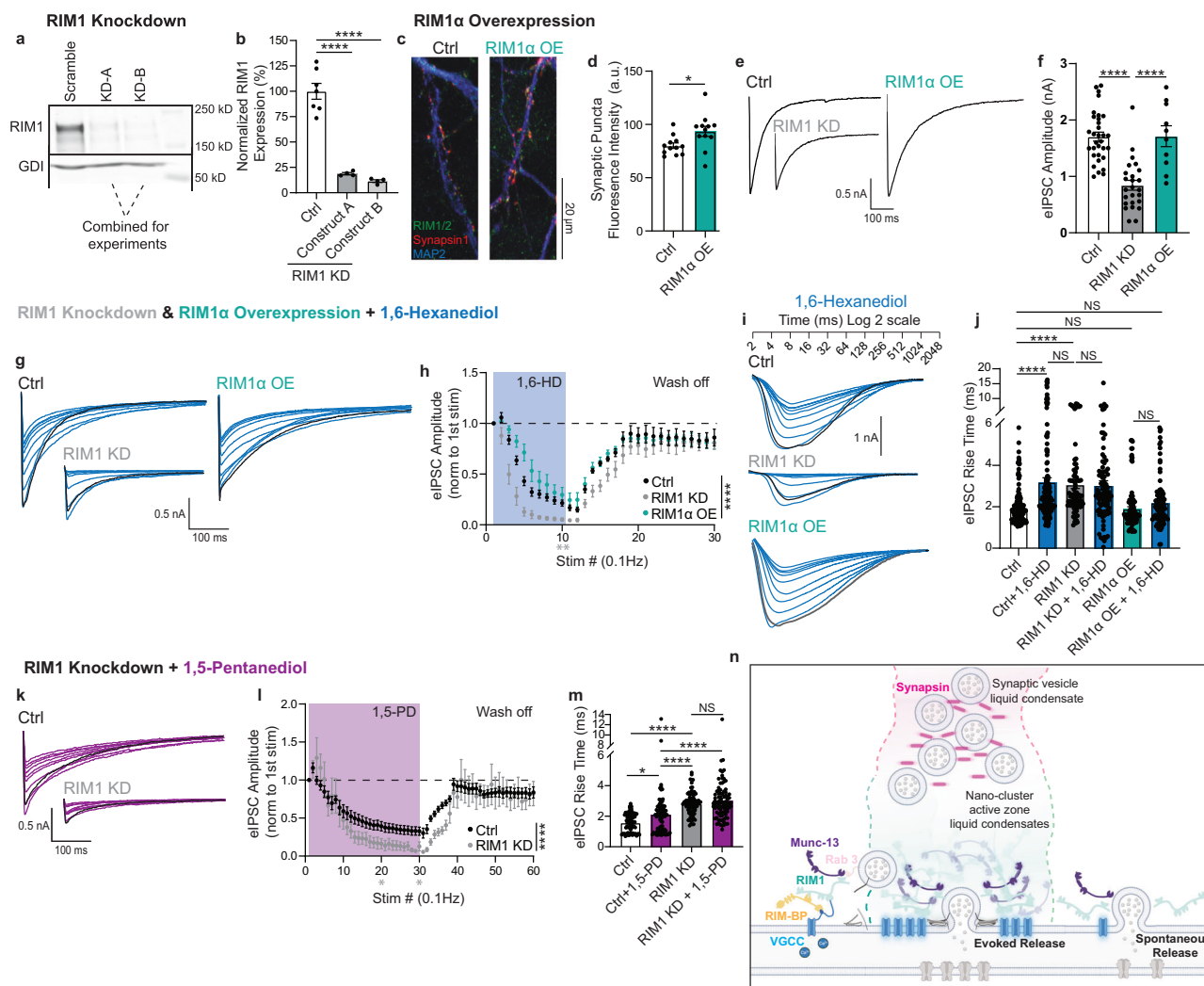


Fig. 6 | Phase separation of RIM1 regulates the efficacy and integrity of fast evoked calcium-dependent release. **a** Example image of RIM1 western blot. **b** RIM1 protein expression normalized to GDI loading control and scramble (ctrl) (A and B RIM1-KD constructs combined for all further experiments) (ctrl $n = 7$, RIM1-KD-A $n = 4$, RIM1-KD-B $n = 4$ samples, quantitative comparisons were made between samples on different gels/blots.). **c** Synapse staining (images are maximum intensity projections from z-stacks). **d** Fluorescence intensity of synaptic puncta (colocalization of RIM1/2 and synapsin1) (ctrl $n = 12$, RIM1α OE $n = 12$ ROIs). **e** Representative traces of basal eIPSCs. **f** eIPSC amplitude (ctrl $n = 32$, RIM1 KD $n = 25$, RIM1α OE $n = 10$ cells). **g** Representative traces of eIPSCs during 3% 1,6-HD wash on, first trace in black. **h** eIPSC amplitude during treatment (comparing nonlinear fit during drug wash on and average amplitudes compared between groups at every 10th stim, ctrl $n = 17$, RIM1 KD $n = 9$, RIM1α OE $n = 10$ cells). **i** Sample traces of eIPSC kinetics following 3% 1,6-HD treatment, first stimulation in black. **j** Analysis of eIPSC rise times (20–80%) (1st 10 stim of treatment or baseline per cell included) (ctrl $n = 170$, RIM1 KD $n = 90$, RIM1α OE = 100 stimulation events). **k** Representative traces of eIPSCs during treatment, first trace in black. **l** eIPSC

amplitude during treatment (comparing nonlinear fit during drug wash on and average amplitudes compared between groups at every 10th stim, ctrl $n = 9$, RIM1 KD $n = 9$ cells). **m** Analysis of eIPSC rise times (20–80%) (1st 10 stim of treatment or baseline per cell included) (ctrl $n = 90$, RIM1 KD $n = 90$ stimulation events). **n** Summary figure of hypothesized pre-synaptic organization; vesicle pool organization relies on LLPS for adequate exocytosis and endocytosis dynamics, evoked release is located within active zone nano-cluster liquid condensates, necessary for VGCC clustering, whereas spontaneous release is located outside liquid RIM1 nano-clusters (Created in BioRender. Guzikowski, N. (2023)). Values are mean \pm SEM. Significance reported as: * $p < 0.05$, ** $p < 0.01$, *** $p < 0.001$, and **** $p < 0.0001$. Statistical analyses conducted were one-way ANOVA with Dunnett's/Tukey's multiple comparison test (**b**, **f**), two-tailed Unpaired t test (**d**, **l**), one-way Kruskal-Wallis test with Dunn's multiple comparisons test (**m**, **h**, **j**), Nonlinear fit (one phase decay) comparison of fit – extra sum-of-squares F test (**h**, **l**), and two-tailed Mann Whitney test (**l**). Source data are provided as a source data file. Exact p -values reported in Supplementary Data 1.

subsequent evoked Ca^{2+} -dependent fusion (Fig. 5l–s)^{52,56,62,63}. Interestingly, the functional phenotype observed here upon LLPS disruption in eIPSC kinetics, RRP size, release probability, and reduced pre-synaptic Ca^{2+} signal closely mimics that of RIM1/2 deletion^{52,69}.

To further test whether the phase separation of RIM1/2 is driving the main functional deficits observed, we perform a molecular knock down of RIM1 (primary isoform expressed) (Fig. 6a, b, Supplementary Fig. 9a, b) and RIM1α overexpression (OE) in primary hippocampal cultures (Fig. 6c,d). Upon RIM1 knockdown, we see a robust phenotype consistent with a RIM1/2 cDKO of decreased eIPSC amplitude and

increased rise time (Fig. 6e,f,j)^{52,69}, with no change in the frequency or kinetics of mEPSCs (Supplementary Fig. 9c–e). In the RIM1α OE we observe no basal effects on eIPSC amplitude or rise time (Fig. 6e,f,j).

To directly ascertain if synaptic nano-organization mediated by RIM1 phase separation is driving the differential dependence of evoked vs. spontaneous release on LLPS, we treated control, RIM1 KD, and RIM1α OE neurons with 3% 1,6-HD. Upon 3% 1,6-HD treatment we see an expected decrease in eIPSC amplitude, yet it is more robust in the RIM1 KD background and decays at a slower rate in the RIM1α OE background (Fig. 6g, h). Furthermore, in the RIM1 KD system the

slowing of eIPSCs with 1,6-HD is occluded, to the extent that Ctrl + 1,6-HD, RIM1 KD, and RIM1 KD + 1,6-HD have equivalent rise times (Fig. 6i,j), suggesting the liquid-like nature of RIM1 is maintaining active zone organization, maintaining the fidelity of evoked release. Interestingly the exogenous increase of RIM1 α at the pre-synapse prevents the 1,6-HD induced slowing of evoked release kinetics (Fig. 6i,j), displaying a resilience to LLPS perturbation due to a potential change in the properties of the condensed phase^{2,70,71}. These results are paralleled by 1,5-PD treatment, where eIPSC amplitude decays to a greater degree in the RIM1 KD background compared to control, and the effect of 1,5-PD treatment on release kinetics is occluded in the RIM1 KD background (Fig. 6k–m).

The combination of results in RIM1 KD and RIM1 α OE neurons reveals the dynamic and specific protein-protein interactions at play that mediate the liquid-like nature of the active zone. In RIM1 KD neurons, interactions with all binding partners (Rab3, Munc13, VGCCs, ELKS, PIP2, RIM-BP, and Liprin) are disrupted, in addition to the phase separation behavior of RIM1²². Therefore, it is expected that the RIM1-KD electrophysiological phenotype is more severe than 1,6-HD or 1,5-PD treatment alone. Whereas in the RIM1 α OE neurons, we hypothesize excess RIM1 at the synapse is disrupting the equilibrium of active zone condensation, which potentially exists under a delicate balance transitioning between a one-phase, two-phase, gel-like or solid-like state². Furthermore, interactions driven by IDRs can be disrupted in protein rich environments shifting the equilibrium from liquid like condensates to gel or solid like complexes^{22,70,71}. The occlusion of augmented eIPSC rise times in the RIM1 KD neurons and the prevention of the slowing of evoked events in the RIM1 α OE neurons suggests that the main driver of the efficacy and integrity of evoked release is the nanoscale phase separation of RIM1 at the active zone (Fig. 6n).

Discussion

Eukaryotic cells rely on intracellular membranes to separate intra-organellar space from the cytosol, ultimately facilitating specialization via compartmentalization. However, despite being the epitome of a highly specialized, ordered, and compartmentalized structure, the synapse lacks a bounding membrane. The nano-scale regulation of numerous, distinct signaling pathways supports the functional diversity of a single synapse, vital in all aspects of human life. LLPS is emerging as a key chemical paradigm to explain synaptic protein interactions due to its dynamic nature, however, whether it is vital, or even necessary, for synaptic signaling remains unknown.

Our data demonstrate that upon acute LLPS disruption, Ca²⁺ mediated action potential-dependent release is dysregulated, while, remarkably, spontaneous neurotransmission, despite its partial reliance on Ca²⁺ signaling, is relatively unaffected⁴⁸. Given that proteins involved in every step of neurotransmission (synaptic vesicle pool clustering^{3,18–20}, active zone scaffolding^{22,23}, active zone assembly²⁴, synaptic vesicle endocytosis^{25,26}, and inhibitory and excitatory postsynaptic density scaffolding^{27–29}) have phase separation properties, these results suggest liquid condensates have spatial and functional specificity. While it is difficult to disrupt global neuronal phase separation and reduce the functional phenotype to one protein complex, our data suggests that most of the characterized synaptic deficit in action potential-dependent neurotransmission is due to the phase separation of active zone nanoclusters. Thus, establishing that within the single micron of the synapse, an immense degree of spatial and functional specificity is supported via the phase separation of RIM1 and subsequent tethering of VGCCs in nanoclusters at the active zone, essential in regulating the efficacy and integrity of fast evoked Ca²⁺-dependent release (Fig. 6n). Importantly, our results demonstrate that despite their large micrometer sized organization *in vitro*, synaptic condensates operate within the nanometer level organization of the synapse to direct evoked release.

Despite 1,6-HD's documented deleterious effects on a broad spectrum of cellular processes, we see our functional effect is not specific to just one aliphatic alcohol (and therefore individual aliphatic alcohol hydrophobicity)^{10,15,72}. Furthermore, despite global LLPS disruption, we detect disruption of only the evoked mode of neurotransmission while spontaneous transmission is largely left intact, supporting the specificity of aliphatic alcohol manipulation rather than a conglomerate of off-target effects. Taken together with the fact that both modes of release occur within the single micron of the synapse, nanoscale alternations that selectively dysregulate evoked neurotransmission highlight the specificity of 1,6-HD action. Lastly, the use of PFA to fix cells has been documented to alter the appearance of phase separation behavior in cells⁷³, therefore, the degree to which nanoscale active zone organization mediated by phase separation is preserved following fixation is unknown. All in all, chemical LLPS manipulation with aliphatic alcohols in combination with both the knock down and overexpression of RIM1 demonstrates how the phase separation property of RIM1 contributes to the complex dynamics of evoked release timing and efficacy.

While the detailed functional deficits in neurotransmission can be attributed to pre-synaptic protein complexes, this does not exclude the potential utility of post-synaptic liquid condensates in other signaling pathways. Beyond the observations described here in basal neurotransmission, the dynamic nature of liquid condensates could be essential in different forms of plasticity, where vesicle cycling, phosphorylation cascades, post-synaptic receptor insertion and internalization are employed. Furthermore, certain protein complexes, including both the excitatory and inhibitory postsynaptic density, might be more resilient to 1,6-HD LLPS perturbation due 1,6-HD's specificity towards hydrophobic LLPS interactions¹⁰, redundant structured domain interactions or the developmental regulation of their liquid properties²⁴. Further demarcation of the functional specificity of LLPS complexes will be instrumental in elucidating the nano-environment of the synapse, essential to both uncovering mechanisms underlying neurological diseases and their treatment^{74,75}.

The specificity of our manipulation to LLPS mediated complexes, independent of targeted structured protein domain interactions, protein trafficking, and genetic perturbations, establishes the nano-specificity and physiological relevance of LLPS. The conservation of fundamental principles from liquid condensate biology to the nano-organization of the synapse demonstrates how a multitude of protein interactions work in synchrony to compartmentalize the synapse into distinct signaling zones. Taken together, the organization of the pre-synaptic milieu, including both synaptic vesicle pools and active zone scaffolding complexes, is fluid in nature, where dynamic liquid condensates are essential for efficient and precise neurotransmission.

Methods

Primary hippocampal culture

Primary hippocampal cultures were prepared from P1/2 rat pups following standard protocols^{76,77}. Postnatal day 1–2 wildtype rat pups were used for all experiments regardless of sex. On average, 2–4 postnatal rat pups were used for each set of cultures with neurons combined across animals. To generate dissociated hippocampal cultures, postnatal pups undergo rapid decapitation at the head/neck junction with surgical scissors. Briefly, hippocampi were dissected from each hemisphere in 20% FBS containing Hank's balanced salt solution. The tissue was then treated with 10 mg/mL of trypsin and 0.5 mg/mL DNase solution for 10 minutes at 37 °C. Following trypsinization, tissue was mechanically dissociated with 0.5 mg/mL DNase and spun down at 250 RCF for ten minutes to isolate a cell pellet. Neurons were resuspended in plating media and plated 1 pup per 10 coverslips coated 50:1 MEM:Matrigel, No. 0 glass coverslips for electrophysiology and confocal imaging, and No. 1.5 MatTek glass bottom dishes for dSTORM. Neurons were incubated for the first 24 hrs in

plating media containing MEM (no phenol red), 5 g/D-glucose, 0.2 g/L NaHCO₃, 0.1 g/L transferrin, 10% FBS, 2 mM L-glutamine and 20 mg/L insulin. 24 hours later, media was changed to growth media with 5% FBS, 0.5 mM L-glutamine, no insulin, and the addition of B27 supplement and 4 mM cytosine arabinoside. On DIV 4, growth media was changed to contain 2 mM cytosine arabinoside. Neurons were maintained in incubators until DIV 14–18 at 5% CO₂ 37 °C.

All experiments involving animals were conducted in accordance with Institutional Animal Care and Use Committee (Protocol ID: M1800103-02) guidelines and procedures at Vanderbilt University.

Drug treatments

Drug treatments used in experiments include 1,6-hexanediol (Sigma Aldrich 240117), 2,5-hexanediol (Sigma Aldrich H11904), 1,6-hexanedithiol (Sigma Aldrich H12005), 1,7-Heptanediol (Millipore Sigma H2201), 1,5-Pentanediol (Thermo Scientific AC129951000) at 3% mass to volume ratio (unless otherwise stated), bis-ANS (4,4'-Dianilino-1,1'-Binaphthyl-5,5'-Disulfonic Acid, Dipotassium Salt) (Thermo Fisher Scientific B153) at 100 μ M, and folimycin at 67 nM (abcam ab144227). Aliphatic alcohol treatment lengths are denoted in figures or figure captions for electrophysiology experiments. Aliphatic alcohol treatment was 1 minute for all dSTORM and live GCaMP imaging experiments.

Immunocytochemistry

Immunocytochemistry was performed on DIV14–18 hippocampal cultures following standard protocols⁷⁶. Briefly, samples were treated with 1,6-HD, then rapidly fixed with 4% PFA 4% sucrose solution for 20 minutes at RT (first 2 minutes of fixation contained 1,6-HD in fixation buffer). Cells were permeabilized with 0.2% Triton-X for 30 minutes at RT, and subsequently blocked with a 2% BSA 1% goat serum 1% donkey serum blocking solution. Samples were then incubated in primary antibody overnight at 4 °C at the following concentrations: anti-SC35 (1:500 abcam ab11826, lot: GR3410532-1), anti-VGluT (1:500 Synaptic Systems 135 304, lot: 1-52), anti-VGAT (1:500 Synaptic Systems 131 004, lot: 3-47), anti-Munc13 (1:250 Synaptic Systems 126 103, lot: 2-35), anti-RIM1/2 (1:500 Synaptic Systems 140 205, lot: 1-5), anti-MAP2 (1:1000 Synaptic Systems 188 004 lot:6-49, 1:500 Synaptic Systems 188 011), anti-Gephyrin (1:150 Synaptic Systems 147 021), anti-PSD95 (1:200 Synaptic Systems 124 011, lot 1-23), anti-Synapsin1 (1:500 Synaptic Systems 106 103, lot 1-17). The following day the samples were incubated in respective secondary antibodies AF647 or CF568 (for dSTORM) and AF568 or AF488 (for confocal) for 90 minutes at RT (AF647 anti-rabbit: Invitrogen A31573, lot: 2359136; CF568 anti-rabbit: Biotium 20803, lot: 21C1022; CF568 anti-guinea pig Biotium 20492, lot:19C0617; AF647 anti-guinea pig: Invitrogen A21450, lot: 2231672; AF568 anti-mouse: Invitrogen A11004, lot: 2090670; AF488 anti-guinea pig: Invitrogen A11073, lot: 2160428). For nuclear speckle staining, coverslips were then incubated with DAPI (1:1000 Roche 10236276001) for five minutes. For confocal microscopy, No. 0 glass coverslips were then mounted on glass slides with aqua-polymount and stored for up to one week at 4 °C in the dark until imaging. For dSTORM microscopy, samples went through a 20 minute post-staining fixation with the 4% PFA 4% sucrose solution and were stored in sample storage buffer for up to one month at 4 °C in the dark until imaging.

Confocal microscopy

For confocal microscopy imaging, z-stacks were collected with a Nikon A1r resonant scanning Eclipse Ti2 HD25 confocal microscope with a 60x (Nikon #MRD01605, CFI60 Plan 765 Apochromat Lambda, N.A. 1.4) objective. NIS-Elements AR v4.5 acquisition software was used for microscope operation and the creation of image maximum intensity projections for analysis. For confocal microscopy synapse imaging, z-stacks were collected with a Zeiss LSM 710 microscope with a 63x objective. Zeiss ZEN microscopy software was used for microscope

operation, acquisition and creation of image maximum intensity projections for analysis. Laser strength and acquisition parameters were consistent throughout entire experiments. Nuclear speckle and synaptic puncta density, size, and fluorescence intensity were analyzed using ImageJ and Intellicount⁷⁸.

dSTORM microscopy

To conduct dSTORM imaging, a Vutara VXL Comprehensive Workstation (microscope and software) was used for image acquisition, single molecule localization, and analysis. Imaging was conducted with 405 nm, 555 nm, and 640 nm excitation lasers with biplane illumination, a 60x objective (1.3 NA, silicone oil), and a sCMOS (scientific Complementary metal–oxide–semiconductor) detector. Samples were imaged in dSTORM imaging buffer which included Cysteamine (MEA), Glucose Oxidase and Catalase for a maximum of two hours at room temp^{76,79}.

Sequential imaging of the 640 channel then the 555 channel was conducted taking 20,000 images per channel. Two color imaging was performed with the protein of interest always imaged in the far-red channel with AF647, as it is an excellent fluorophore for dSTORM. Images were taken at 50 frames per seconds (20 ms exposure time) of single z-planes at 2 μ m thickness and field of view 50 μ m \times 50 μ m. For fluorophore localization, 3D measured point spread functions collected during microscope calibration with B-Spline PSF Interpolation method PSF fitting of localizations was used.

The following combinations of antibodies were imaged together:

647: RIM1/2 (Synaptic Systems 140 205) with 568: Munc13 (Synaptic Systems 126 103)

647: Munc13 (Synaptic Systems 126 103) with 568: VGluT (Synaptic Systems 135 304)

647: VGAT (Synaptic Systems 131 004) with 568: Gephyrin (Synaptic Systems 147 021)

647: VGluT (Synaptic Systems 135 304) with 568: PSD95 (Synaptic Systems 124 011)

The Vutara VXL Comprehensive Workstation software was used for all dSTORM analysis conducted. To define synaptic clusters of individual proteins DBScan, Density-Based Spatial Clustering of Application with Noise, was used with the following parameters: maximum particle distance of 0.1 μ m, minimum particle count of 30, and surface hull α shape radius of 0.15 μ m. Following the classification of VGluT, VGAT, Munc13, and RIM1/2 single molecule localizations into individual clusters, cluster volume and sphericity were calculated. To define Munc13 and RIM1/2 nanoclusters pair correlation functions were generated for individual clusters. Ten synaptic clusters from each ROI imaged were selected at random for analysis. Pair correlation functions were normalized to theoretical fits to account for cluster density and shape differences to ultimately provide a measure of sub-synaptic clustering^{80,81}. The Vutara VXL Comprehensive Workstation software was used to create example dSTORM images displaying single molecule localizations.

Electrophysiology – whole cell patch clamp

Whole cell patch clamp electrophysiology was performed with a CV203BU head stage, Axopatch 200B amplifier, Digidata 1320 digitizer, and 8 Clampex 8.0 software (Molecular Devices). Whole cell patch clamp recordings were filtered at 1 kHz and sampled at 100 μ s. 3–6 M Ω borosilicate glass patch pipettes were used for all recordings and cells were held at 70 mV for voltage clamp experiments. For patch clamp experiments external bath solution contained 150 mM NaCl, 4 mM KCl, 10 mM D-glucose, 10 mM HEPES, 1.25 mM MgCl₂, and 2 mM CaCl₂ at pH 7.4 and 320 mOsm. For 8 mM Ca²⁺ bath solution NaCl concentration was slightly decreased to maintain solution osmolarity. To isolate mIPSCs TTX (1 μ M), APV (50 μ M), and CNQX (10 μ M) were included in the bath solutions. To isolate mEPSCs TTX (1 μ M), APV (50 μ M), and bicuculline (20 μ M) were added to the bath. To isolate eIPSCs APV

(50 μ M) and CNQX (10 μ M) were added to the bath. To isolate eEPSCs APV (50 μ M) and bicuculline (20 μ M) were added to the bath. A parallel bipolar electrode provided field stimulation (35 mA) for evoked recordings. Evoked recordings were conducted at a gain of 1x, resulting in quantization of amplitudes such that some amplitude measurements in source data are identical despite being collected from different traces and having distinct kinetic characteristics (e.g. rise and decay times). For current clamp recordings no additional drugs were included in the bath. Current clamp step protocol consisted of 45 Steps at $\Delta 10$ pA from 100 pA to +340 pA.

For voltage clamp experiments internal pipette solution contained 115 mM Cs-MeSO₃, 10 mM CsCl, 5 mM NaCl, 10 mM HEPES, 0.6 mM EGTA, 20 mM tetraethylammonium-Cl, 4 mM Mg-ATP, 0.3 mM Na₃GTP, and 10 mM QX-314 [N-(2,6-dimethylphenylcarbamoylmethyl)-triethylammonium bromide] at pH 7.35 and 300 mOsm. For current clamp experiments internal solution contained 110 mM K-Gluconate, 20 mM KCl, 10 mM NaCl, 10 mM HEPES, 4 mM Mg-ATP, 0.3 mM Na₃GTP, and 0.6 mM EGTA at pH 7.3 and 284 mOsm.

Lentiviral infection/transfection

Lentivirus was made by transfecting HEK 293 cells with three packaging plasmids pCMV-VSV-G, pMDLg/pRRE, and pRSV-Rev at 0.5 μ g each, and the plasmid of interest pFUW at 1 μ g, Syt 1 KD at 1 μ g, SNAP25 L50S at 1 μ g, or SNAP25 D166Y at 1 μ g with FuGENE 6. For RIMI KD experiments shRNA sequences RIMI-KD-A at 1 μ g, RIMI-KD-B at 1 μ g, or a random control sequence at 1 μ g were used with the above packaging plasmids. RIMI-KD-A and RIMI-KD-B constructs were combined in the same FuGENE/DNA mix. shRNA plasmid DNA sequences; XXE-rRIMI-KD-A: 4383 gggcgatattccaaatcgggaggaggata, XXE-rRIMI-KD-B: 4674 ggggtgtggctcaaatctgttgaagaac, random control: gcattaccagagctaactcagatagtact. For RIMI α overexpression experiments 1.5 μ g of DNA was used. HEK media was changed to neuronal growth media 24 hours post-transfection and then lentivirus collected 48 hours later. Lentivirus was spun down at 690 RCF for 15 minutes and then 200 μ l of pFUW, Syt1 KD, SNAP25 L50S, SNAP25 D166Y, RIMI-KD, RIMI α or random control sequence lentivirus was added to neuronal media on DIV4.

Live imaging and analysis

Calcium-phosphate transfection was used to sparsely transfect hippocampal cultures with Syb2-GCaMP8s and soluble GCaMP8f. Per well of a 24-well plate a precipitate was formed by combining 1 μ g of Syb2-GCaMP8s or GCaMP8f plasmid DNA, 2 μ l of 2 M CaCl₂, 13 μ l ddH₂O with 15 μ l of 2 \times N-2-Hydroxyethylpiperazine-N'-2-Ethanesulfonic Acid (HEPES) dropwise (brief vortex in between each drop). The solution was incubated at RT for 15 minutes and then 30 μ l added to each well of a 24-well plate where growth media was removed and replaced with 1 mL MEM. Neurons were incubated with precipitate for 30 minutes in the incubator and then washed twice with 1 mL of MEM and then the original growth media replaced back into the well.

Live imaging was conducted on DIV15-16, seven days post transfection. A Nikon Eclipse TE2000-U microscope with a 60x Plan Apo objective, a Lambda-DG4 (Sutter instruments) with a GFP filter, and EMCCD camera. Acquisition rate was 10 Hz, no binning. Fluorescence activity was recorded throughout the length of experiment protocol.

External bath solution contained 150 mM NaCl, 4 mM KCl, 10 mM D-glucose, 10 mM HEPES, 1.25 mM MgCl₂, 2 mM CaCl₂, at pH 7.4 and APV (50 μ M) and CNQX (10 μ M) to prevent recurrent activity. 90 mM K⁺ solution perfusion was used to help isolate ROIs during analysis.

Fluorescence intensity over time was analyzed by the selection of pre-synaptic ROIs using a custom-made macro for Fiji. High potassium induced fluorescence peaks were isolated using a custom Matlab (Mathworks) script based on our lab's previous imaging analysis⁸². The script was used to detect and analyze fluorescent peaks representing presynaptic Ca²⁺ transients in synaptic ROIs.

Western blot

Protein was collected from primary hippocampal cultures infected with scramble control, RIMI-KD-A, and RIMI-KD-B plasmids in lysis buffer containing Lamelli buffer (2x), 2-Mercaptoethanol, and protease and phosphatase inhibitors (phosSTOP and cOmplete tablets, mini (Roche)).

Samples were sonicated for 40 minutes then heated at 40 °C for ten minutes. Samples were loaded into a 7% SDS-PAGE gel and run for ~3 hrs at 60 volts. Protein was then transferred with a Trans-Blot Turbo Transfer System to a nitrocellulose membrane. Samples were blocked in 5% milk in Tris-Buffered saline (TBS) for 1 hr. Membranes were then incubated overnight in rabbit anti-RIMI (Synaptic systems 140 003, 1:5000) and mouse anti-GDI (loading control) (Synaptic systems 130 011, 1:5000) diluted in 5% milk at 4 °C overnight.

The following day membranes were then washed 3 x in TBS for 10 minutes. Membranes were then incubated in secondary antibody goat anti-rabbit (LiCOR 926-32211) and goat anti-mouse (LiCOR 926-32210) diluted in 5% milk for 1 hr. Following secondary antibody incubation membranes were washed 3 x in TBS for 10 min. Membranes were imaged with the Odyssey Clix imaging system (Li-Cor). Band intensities were calculated using image J and normalized to their respective loading control and then scramble control.

Statistical analysis

mPSC frequencies, amplitudes, and kinetics were analyzed using Mini Analysis software (Synaptosoft), ePSCs and action potentials were analyzed with Clampfit 10.3 (Molecular Devices). GraphPad Prism 9 was used to conduct all analysis. First a Shapiro-Wilk test for normality was run to select the appropriate parametric or nonparametric statistical analysis to compare groups. When comparing two groups a paired or unpaired t-test or nonparametric Mann Whitney test was conducted. When comparing three or more groups a one-way ANOVA or nonparametric Kruskal-Wallis test or Friedman test with Tukey, Dunnett, or Dunn's post hoc multiple comparisons tests was conducted as appropriate. A Kolmogorov-Smirnov test was used to compare cumulative probability histograms. $p < 0.05$ was considered statistically significant. Data presented as mean \pm standard error of mean (SEM). Please refer to Supplemental Data 1 for individual tests run for each figure panel.

Reporting summary

Further information on research design is available in the Nature Portfolio Reporting Summary linked to this article.

Data availability

Any reagents or plasmids are available upon request from the corresponding author. Source data are provided with this paper.

Code availability

Custom Matlab script is already published in Wang et al.⁴⁸.

References

1. Brangwynne, C. P. et al. Germline P granules are liquid droplets that localize by controlled dissolution/condensation. *Science* **324**, 1729–1732 (2009).
2. Chen, X., Wu, X., Wu, H. & Zhang, M. Phase separation at the synapse. *Nat. Neurosci.* **23**, 301–310 (2020).
3. Wu, X., Qiu, H. & Zhang, M. Interactions between membraneless condensates and membranous organelles at the presynapse: a phase separation view of synaptic vesicle cycle. *J. Mol. Biol.* **435**, 167629 (2023).
4. McDonald, N. A. & Shen, K. Finding functions of phase separation in the presynapse. *Curr. Opin. Neurobiol.* **69**, 178–184 (2021).
5. Lyon, A. S., Peeples, W. B. & Rosen, M. K. A framework for understanding functions of biomolecular condensates on molecular to cellular scales. *Nat. Rev. Mol. Cell Biol.* **22**, 215 (2021).

6. Li, P. et al. Phase transitions in the assembly of multi-valent signaling proteins. *Nature* **483**, 336–340 (2012).
7. Mittag, T. & Parker, R. Multiple modes of protein–protein interactions promote RNP granule assembly. *J. Mol. Biol.* **430**, 4636–4649 (2018).
8. van der Lee, R. et al. Classification of intrinsically disordered regions and proteins. *Chem. Rev.* **114**, 6589–6631 (2014).
9. Milovanovic, D. & De Camilli, P. Synaptic vesicle clusters at synapses: a distinct liquid phase? *Neuron* **93**, 995–1002 (2017).
10. Berkeley, R. F. & Debelouchina, G. T. Chemical tools for study and modulation of biomolecular phase transitions. *Chem. Sci.* **13**, 14226–14245 (2022).
11. Pappu, R. V., Cohen, S. R., Dar, F., Farag, M. & Kar, M. Phase transitions of associative biomacromolecules. *Chem. Rev.* **123**, 8945–8987 (2023).
12. Mittag, T. & Pappu, R. V. A conceptual framework for understanding phase separation and addressing open questions and challenges. *Mol. Cell* **82**, 2201–2214 (2022).
13. McSwiggen, D. T., Mir, M., Darzacq, X. & Tjian, R. Evaluating phase separation in live cells: diagnosis, caveats, and functional consequences. *Genes Dev.* **33**, 1619–1634 (2019).
14. Kroschwald, S., Maharana, S. & Simon, A. Hexanediol: a chemical probe to investigate the material properties of membrane-less compartments. *Matters* <https://doi.org/10.19185/matters.201702000010> (2017).
15. Lin, Y. et al. Toxic PR poly-dipeptides encoded by the C9orf72 repeat expansion target LC domain polymers. *Cell* **167**, 789–802.e12 (2016).
16. Ribbeck, K. & Görlich, D. The permeability barrier of nuclear pore complexes appears to operate via hydrophobic exclusion. *EMBO J.* **21**, 2664–2671 (2002).
17. Banani, S. F., Lee, H. O., Hyman, A. A. & Rosen, M. K. Biomolecular condensates: organizers of cellular biochemistry. *Nat. Rev. Mol. Cell Biol.* **18**, 285–298 (2017).
18. Milovanovic, D., Wu, Y., Bian, X. & De Camilli, P. A liquid phase of synapsin and lipid vesicles. *Science* **361**, 604–607 (2018).
19. Park, D. et al. Cooperative function of synaptophysin and synapsin in the generation of synaptic vesicle-like clusters in non-neuronal cells. *Nat. Commun.* **12**, 263 (2021).
20. Park, D. et al. Synaptic vesicle proteins and ATG9A self-organize in distinct vesicle phases within synapsin condensates. *Nat. Commun.* **14**, 455 (2023).
21. Pechstein, A. et al. Vesicle Clustering in a Living Synapse Depends on a Synapsin Region that Mediates Phase Separation. *Cell Rep.* **30**, 2594–2602.e3 (2020).
22. Wu, X. et al. RIM and RIM-BP Form Presynaptic Active-Zone-like Condensates via Phase Separation. *Mol. Cell* **73**, 971–984.e5 (2019).
23. Emperador-Melero, J. et al. PKC-phosphorylation of Liprin- α 3 triggers phase separation and controls presynaptic active zone structure. *Nat. Commun.* **12**, 3057 (2021).
24. McDonald, N. A., Fetter, R. D. & Shen, K. Assembly of synaptic active zones requires phase separation of scaffold molecules. *Nature* **588**, 454–458 (2020).
25. Day, K. J. et al. Liquid-like protein interactions catalyze assembly of endocytic vesicles. *Nat. Cell Biol.* **23**, 366–376 (2021).
26. Imoto, Y. et al. Dynamin is primed at endocytic sites for ultrafast endocytosis. *Neuron* **110**, 2815–2835.e13 (2022).
27. Zeng, M. et al. Reconstituted postsynaptic density as a molecular platform for understanding synapse formation and plasticity. *Cell* **174**, 1172–1187.e16 (2018).
28. Zeng, M. et al. Phase separation-mediated TARP/MAGUK complex condensation and AMPA receptor synaptic transmission. *Neuron* **104**, 529–543.e6 (2019).
29. Bai, G., Wang, Y. & Zhang, M. Gephyrin-mediated formation of inhibitory postsynaptic density sheet via phase separation. *Cell Res.* **31**, 312–325 (2021).
30. Babinchak, W. M. et al. Small molecules as potent biphasic modulators of protein liquid-liquid phase separation. *Nat. Commun.* **11**, 5574 (2020).
31. Atasoy, D. et al. Spontaneous and evoked glutamate release activates two populations of NMDA receptors with limited overlap. *J. Neurosci.* **28**, 10151–10166 (2008).
32. Guzikowski, N. J. & Kavalali, E. T. Nano-organization of spontaneous GABAergic transmission directs its autonomous function in neuronal signaling. *Cell Rep.* **40**, 111172 (2022).
33. Melom, J. E., Akbergenova, Y., Gavornik, J. P. & Littleton, J. T. Spontaneous and evoked release are independently regulated at individual active zones. *J. Neurosci.* **33**, 17253–17263 (2013).
34. Peled, E. S., Newman, Z. L. & Isacoff, E. Y. Evoked and Spontaneous Transmission Favored by Distinct Sets of Synapses. *Curr. Biol.* **24**, 484–493 (2014).
35. Reese, A. L. & Kavalali, E. T. Single synapse evaluation of the post-synaptic NMDA receptors targeted by evoked and spontaneous neurotransmission. *eLife* **5**, e21170 (2016).
36. Sara, Y., Bal, M., Adachi, M., Monteggia, L. M. & Kavalali, E. T. Use-dependent AMPA receptor block reveals segregation of spontaneous and evoked glutamatergic neurotransmission. *J. Soc. Neurosci.* **31**, 5378–5382 (2011).
37. Horvath, P. M., Piazza, M. K., Monteggia, L. M. & Kavalali, E. T. Spontaneous and evoked neurotransmission are partially segregated at inhibitory synapses. *eLife* **9**, e52852 (2020).
38. Guzikowski, N. J. & Kavalali, E. T. Nano-organization at the synapse: segregation of distinct forms of neurotransmission. *Front. Synaptic Neurosci.* **13**, 111172 (2021).
39. Gitler, D. et al. Different presynaptic roles of synapsins at excitatory and inhibitory synapses. *J. Neurosci.* **24**, 11368–11380 (2004).
40. Alten, B. et al. Role of aberrant spontaneous neurotransmission in SNAP25-associated encephalopathies. *Neuron* **109**, 59–72.e5 (2021).
41. Sara, Y., Virmani, T., Deák, F., Liu, X. & Kavalali, E. T. An isolated pool of vesicles recycles at rest and drives spontaneous neurotransmission. *Neuron* **45**, 563–573 (2005).
42. Ertunc, M. et al. Fast synaptic vesicle reuse slows the rate of synaptic depression in the CA1 region of hippocampus. *J. Neurosci.* **27**, 341–354 (2007).
43. Alabi, A. A. & Tsien, R. W. Synaptic vesicle pools and dynamics. *Cold Spring Harb. Perspect. Biol.* **4**, a013680 (2012).
44. Qiu, H. et al. Short-distance vesicle transport via phase separation. *Cell* <https://doi.org/10.1016/j.cell.2024.03.003> (2024).
45. Eggermann, E., Bucurenciu, I., Goswami, S. P. & Jonas, P. Nanodomain coupling between Ca²⁺ channels and sensors of exocytosis at fast mammalian synapses. *Nat. Rev. Neurosci.* **13**, 7–21 (2011).
46. Horishita, T. & Harris, R. A. n-Alcohols inhibit voltage-gated Na⁺ channels expressed in *Xenopus* oocytes. *J. Pharmacol. Exp. Ther.* **326**, 270–277 (2008).
47. Armstrong, C. M. & Binstock, L. The effects of several alcohols on the properties of the squid giant axon. *J. Gen. Physiol.* **48**, 265–277 (1964).
48. Wang, C. S., Monteggia, L. M. & Kavalali, E. T. Spatially non-overlapping Ca²⁺ signals drive distinct forms of neurotransmission. *Cell Rep.* **42**, 113201 (2023).
49. Williams, C. et al. Co-activation of multiple tightly-coupled calcium channels triggers spontaneous release of GABA. *Nat. Neurosci.* **15**, 1195–1197 (2012).
50. Goswami, S. P., Bucurenciu, I. & Jonas, P. Miniature IPSCs in Hippocampal granule cells are triggered by voltage-gated Ca²⁺ channels via microdomain coupling. *J. Neurosci.* **32**, 14294–14304 (2012).

51. Hibino, H. et al. RIM - binding proteins (RBPs) couple Rab3 - interacting molecules (RIMs) to voltage - gated Ca²⁺ channels. *Neuron* **34**, 411–423 (2002).
52. Kaeser, P. S. et al. RIM proteins tether Ca²⁺-channels to presynaptic active zones via a direct PDZ-domain interaction. *Cell* **144**, 282–295 (2011).
53. Müller, J. A. et al. A presynaptic phosphosignaling hub for lasting homeostatic plasticity. *Cell Rep.* **39**, 110696 (2022).
54. Wu, X. et al. Vesicle tethering on the surface of phase-separated active zone condensates. *Mol. Cell* **81**, 13–24.e7 (2021).
55. Wang, S. S. H. et al. Fusion competent synaptic vesicles persist upon active zone disruption and loss of vesicle docking. *Neuron* **91**, 777–791 (2016).
56. Betz, A. et al. Functional interaction of the active zone proteins munc13-1 and RIM1 in synaptic vesicle priming. *Neuron* **30**, 183–196 (2001).
57. Yang, X. et al. Syntaxin opening by the MUN domain underlies the function of Munc13 in synaptic-vesicle priming. *Nat. Struct. Mol. Biol.* **22**, 547–554 (2015).
58. Schoch, S. et al. RIM1 α forms a protein scaffold for regulating neurotransmitter release at the active zone. *Nature* **415**, 321–326 (2002).
59. Nair, D. et al. Super-resolution imaging reveals that AMPA receptors inside synapses are dynamically organized in nanodomains regulated by PSD95. *J. Neurosci.* **33**, 13204–13224 (2013).
60. MacGillavry, H. D., Song, Y., Raghavachari, S. & Blanpied, T. A. Nanoscale scaffolding domains within the postsynaptic density concentrate synaptic AMPA receptors. *Neuron* **78**, 615–622 (2013).
61. Fukata, Y. et al. Local palmitoylation cycles define activity-regulated postsynaptic subdomains. *J. Cell Biol.* **202**, 145–161 (2013).
62. Tang, A.-H. et al. A trans-synaptic nanocolumn aligns neurotransmitter release to receptors. *Nature* **536**, 210–214 (2016).
63. Ramsey, A. M. et al. Subsynaptic positioning of AMPARs by LRRTM2 controls synaptic strength. *Sci. Adv.* **7**, eabf3126 (2021).
64. Nakamura, Y. et al. Nanoscale distribution of presynaptic Ca²⁺ channels and its impact on vesicular release during development. *Neuron* **85**, 145–158 (2015).
65. Schmidt, H. et al. Nanodomain coupling at an excitatory cortical synapse. *Curr. Biol.* **23**, 244–249 (2013).
66. Arai, I. & Jonas, P. Nanodomain coupling explains Ca²⁺ independence of transmitter release time course at a fast central synapse. *eLife* **3**, e04057 (2014).
67. Bucurenciu, I., Kulik, A., Schwaller, B., Frotscher, M. & Jonas, P. Nanodomain coupling between Ca²⁺ channels and Ca²⁺ sensors promotes fast and efficient transmitter release at a cortical GABAergic synapse. *Neuron* **57**, 536–545 (2008).
68. Schneggenburger, R. & Neher, E. Presynaptic calcium and control of vesicle fusion. *Curr. Opin. Neurobiol.* **15**, 266–274 (2005).
69. Han, Y., Kaeser, P. S., Südhof, T. C. & Schneggenburger, R. RIM determines Ca²⁺ channel density and vesicle docking at the presynaptic active zone. *Neuron* **69**, 304–316 (2011).
70. Gao, Z. et al. Liquid-Liquid phase separation: unraveling the enigma of biomolecular condensates in microbial cells. *Front. Microbiol.* **12**, 751880 (2021).
71. Feng, Z., Jia, B. & Zhang, M. Liquid-liquid phase separation in biology: specific stoichiometric molecular interactions vs promiscuous interactions mediated by disordered sequences. *Biochemistry* **60**, 2397–2406 (2021).
72. Düster, R., Kaltheuner, I. H., Schmitz, M. & Geyer, M. 1,6-Hexanediol, commonly used to dissolve liquid-liquid phase separated condensates, directly impairs kinase and phosphatase activities. *J. Biol. Chem.* **296**, 100260 (2021).
73. Irgen-Gioro, S., Yoshida, S., Walling, V. & Chong, S. Fixation can change the appearance of phase separation in living cells. *eLife* **11**, e79903 (2022).
74. Zbinden, A., Pérez-Berlanga, M., De Rossi, P. & Polymenidou, M. Phase separation and neurodegenerative diseases: a disturbance in the force. *Dev. Cell* **55**, 45–68 (2020).
75. Wang, B. et al. Liquid-liquid phase separation in human health and diseases. *Signal Transduct. Target. Ther.* **6**, 1–16 (2021).
76. Guzikowski, N. J. & Kavalali, E. T. Super-resolution imaging of synaptic scaffold proteins in rat hippocampal neurons. *STAR Protoc.* **4**, 102080 (2023).
77. Kavalali, E. T., Klingauf, J. & Tsien, R. W. Activity-dependent regulation of synaptic clustering in a hippocampal culture system. *Proc. Natl Acad. Sci. USA* **96**, 12893–12900 (1999).
78. Fantuzzo, J. A. et al. Intellicount: high-throughput quantification of fluorescent synaptic protein puncta by machine learning. *eNeuro* **4**, e0219-17 (2017).
79. Martin, L. et al. A protocol to quantify chromatin compaction with confocal and super-resolution microscopy in cultured cells. *STAR Protoc.* **2**, 100865 (2021).
80. Hartley, J. M. et al. Super-resolution imaging and quantitative analysis of membrane protein/lipid raft clustering mediated by cell-surface self-assembly of hybrid nanoconjugates. *ChemBioChem* **16**, 1725–1729 (2015).
81. Sengupta, P., Jovanovic-Talman, T. & Lippincott-Schwartz, J. Quantifying spatial organization in point-localization super-resolution images using pair correlation analysis. *Nat. Protoc.* **8**, 345–354 (2013).
82. Wang, C. S., Chanaday, N. L., Monteggia, L. M. & Kavalali, E. T. Probing the segregation of evoked and spontaneous neurotransmission via photobleaching and recovery of a fluorescent glutamate sensor. *eLife* **11**, e76008 (2022).

Acknowledgements

We are grateful to Dr. Ok-Ho Shin for his technical assistance in generating the RIM1 shRNA constructs. We are extremely grateful to Drs. Susanne Schoch and Maksim Galkov for the RIM1 α plasmid. We would like to thank the lab of Dr. Richard Sando for the use of their confocal microscope with the help of Dr. Krassimira Garbett. We thank both the Kavalali and Monteggia labs for helpful feedback and insight throughout this project. This research was supported by the NIMH (Grant MH066198 to E.T.K., Grant MH132197-01A1 to N.J.G.).

Author contributions

E.T.K. and N.J.G. conceptualized the study. N.J.G. conducted all experiments and analysis. E.T.K. and N.J.G. wrote and edited the manuscript together.

Competing interests

The authors declare no competing interests.

Additional information

Supplementary information The online version contains supplementary material available at <https://doi.org/10.1038/s41467-024-54423-7>.

Correspondence and requests for materials should be addressed to Ege T. Kavalali.

Peer review information *Nature Communications* thanks the anonymous reviewer(s) for their contribution to the peer review of this work. A peer review file is available.

Reprints and permissions information is available at <http://www.nature.com/reprints>

Publisher's note Springer Nature remains neutral with regard to jurisdictional claims in published maps and institutional affiliations.

Open Access This article is licensed under a Creative Commons Attribution-NonCommercial-NoDerivatives 4.0 International License, which permits any non-commercial use, sharing, distribution and reproduction in any medium or format, as long as you give appropriate credit to the original author(s) and the source, provide a link to the Creative Commons licence, and indicate if you modified the licensed material. You do not have permission under this licence to share adapted material derived from this article or parts of it. The images or other third party material in this article are included in the article's Creative Commons licence, unless indicated otherwise in a credit line to the material. If material is not included in the article's Creative Commons licence and your intended use is not permitted by statutory regulation or exceeds the permitted use, you will need to obtain permission directly from the copyright holder. To view a copy of this licence, visit <http://creativecommons.org/licenses/by-nc-nd/4.0/>.

© The Author(s) 2024